

2D multi-parameter viscoelastic shallow-seismic full waveform inversion: reconstruction tests and first field-data application

Lingli Gao, Yudi Pan, Thomas Bohlen

CRC Preprint 2020/14, April 2020

KARLSRUHE INSTITUTE OF TECHNOLOGY

CRC 1173



Wave
phenomena

Participating universities



Universität Stuttgart

EBERHARD KARLS
UNIVERSITÄT
TÜBINGEN



Funded by

DFG

2D multi-parameter viscoelastic shallow-seismic full waveform inversion: reconstruction tests and first field-data application

Lingli Gao^{1,†}, Yudi Pan^{2,†}, and Thomas Bohlen²

¹ *Institute of Applied and Numerical Mathematics, Karlsruhe Institute of Technology (KIT), Karlsruhe 76131, Germany*

² *Geophysical Institute, Karlsruhe Institute of Technology (KIT), Karlsruhe 76187, Germany*

[†] *The first two authors contributed equally to this work*

SUMMARY

2D full-waveform inversion (FWI) of shallow-seismic wavefields has recently become a novel way to reconstruct S-wave velocity models of the shallow subsurface with high vertical and lateral resolution. In most applications, seismic wave attenuation is ignored or considered as a passive modelling parameter only. In this study, we explore the feasibility and performance of multi-parameter viscoelastic 2D FWI in which seismic velocities and attenuation of P- and S-waves, respectively, and mass density are inverted simultaneously. Synthetic reconstruction experiments reveal that multiple crosstalks between all viscoelastic material parameters may occur. The reconstruction of S-wave velocity is always robust and of high quality. The parameters P-wave velocity and density exhibit weaker sensitivity and can be reconstructed more reliably by multi-parameter viscoelastic FWI. Anomalies in S-wave attenuation can be recovered but with limited resolution. In a field data application, a small-scale refilled trench is nicely delineated as a low P- and S-wave velocity anomaly. The reconstruction of P-wave velocity is improved by the simultaneous inversion of attenuation. The reconstructed S-wave attenuation reveals higher attenuation in the shallow weathering zone and weaker attenuation below. The variations

in the reconstructed P- and S-wave velocity models are consistent with the reflectivity observed in a GPR profile.

Key words: Surface waves and free oscillations; Waveform inversion; Seismic attenuation

1 INTRODUCTION

The reconstruction of near-surface models by using shallow-seismic wavefields plays an important role in geophysical and geotechnical site investigation. Shallow-seismic wavefields are dominated by surface waves, which makes the inversion of them attractive to reconstruct near-surface models. The inversion of surface waves is getting increasingly popular due to their high sensitivity to the S-wave velocity (Socco et al. 2010), which is an important lithological and geotechnical parameter to characterize the composition and stability of sediments.

Most of the current surface-wave methods are based on the extraction and inversion of surface-wave dispersion curves (Xia et al. 1999). The dispersion-based surface-wave methods, however, fail when strong lateral heterogeneity exists, which is regarded as one of their limitations (Pan et al. 2019). Different approaches are proposed to account for lateral heterogeneity, such as laterally constrained inversion (Socco et al. 2009), cross-correlation analysis of multichannel data (Hayashi & Suzuki 2004; Ikeda et al. 2013), and spatial windowing (Bohlen et al. 2004; Bergamo et al. 2012). Another limitation that current surface-wave methods face is the uncertainty in the correct estimation and identification of multi-modal dispersion curves (Boaga et al. 2013; Gao et al. 2014, 2016). Full waveform inversion (FWI) may overcome these limitations and can produce high-resolution multi-parameter models for complex geologic structures. FWI was first introduced by Tarantola (1984) and Mora (1987) in time domain with gradient-based inversion. With the rapid development of computational power, it has become increasingly popular to use 2D FWI of surface wave to reconstruct near-surface models. Romdhane et al. (2011) and Tran et al. (2013) demonstrated the effectiveness of 2D frequency-domain elastic FWI in reconstructing heterogeneous near-surface model. Groos et al. (2014, 2017) and Pan et al. (2016, 2018) showed that 2D time-domain elastic FWI could efficiently delineate shallow subsurface with high resolution. Besides, 3D FWI of the surface wave is also becoming feasible in recent years (Irnaka et al. 2019; Mirzanejad & Tran 2019). FWI of the surface wave is highly ill-posed and might be trapped in local minima, especially for the conventional least-squares misfit. One practical way to mitigate this problem is to use an initial model built by inverting surface-wave dispersion curves. Besides, an alternative objective function, such as amplitude-spectrum-based misfit (Pérez Solano et al. 2014;

Masoni et al. 2016), envelope-based misfit (Wu et al. 2014; Yuan et al. 2015), and multi-objective misfit (Pan et al. 2020), can be used to reduce the nonlinearity of surface-wave FWI.

Besides the velocity model, seismic attenuation also plays a crucial role in subsurface characterization. It mainly influences the amplitude of the seismic wave and would also influence the phase of the seismic wave when strong attenuation exists. Considering the attenuation effect in FWI is becoming an important topic. Many studies are focused on the viscoacoustic FWI, in which P-wave velocity (V_P) and quality factor (Q) can be inverted recursively or simultaneously (Kamei & Pratt 2013; Malinowski et al. 2011; Virieux & Operto 2009). Brossier (2011) showed the potential of multi-parameter viscoelastic FWI by using frequency-domain synthetic examples. Bai et al. (2017) showed the reconstruction of attenuation in anisotropic viscoelastic media. Besides the successful applications of FWI in exploration seismic that are focusing on the utilizing of body waves, there are a few studies which investigate the performance of viscoelastic FWI on the shallow-seismic surface wave. Some previous studies neglected effects of attenuation (Romdhane et al. 2011; Tran et al. 2013; Xing & Mazzotti 2019). Groos et al. (2014) and Mirzanejad & Tran (2019) showed that the effects of anelastic damping must be considered in the shallow-seismic FWI for better reconstruction of a high-resolution S-wave velocity model. Groos et al. (2014) proposed a passive-viscoelastic FWI approach in which a fixed prior estimated Q model is used in the forward solver to account for the viscous effect. The pure elastic and passive-viscoelastic FWI approaches are generally valid when the attenuation is weak and the Q model is laterally homogeneous. However, near-surface materials can be highly heterogeneous and may also exhibit strong spatial variation of strong attenuation. In this case, simply ignoring the viscous effect might deteriorate the reconstruction of S-wave velocity. Furthermore, the Q model is an important additional material parameter and can help to discriminate different lithologies and to improve the petrophysical characterization. This can be of interest in hydrological studies or the estimation of local site amplification due to earthquakes (Xia et al. 2002). Therefore, the reconstruction of multi-parameter models including both velocity and Q models using shallow-seismic surface waves is of great interest.

Solving the viscoelastic wave equation in the time domain usually requires additional memory equations (Carcione et al. 1988; Robertsson et al. 1994; Bohlen 2002). Because the viscoelastic wave equation is not self-adjoint, an adjoint state equation which differs from the viscoelastic wave equation needs to be solved in viscoelastic FWI (Yang et al. 2016; Fabien-Ouellet et al. 2017).

In this paper, we study the performance of 2D multi-parameter viscoelastic FWI applied to shallow seismic wavefields. General theories of the forward simulation and FWI workflow are given in the first section. Synthetic reconstruction tests for spatially correlated and uncorrelated models are performed to investigate the validity of multi-parameter viscoelastic FWI as well as to study the crosstalk between

parameters. Viscoelastic and elastic FWI results are compared to investigate the necessity of including attenuation information. The crosstalk between Q_S and V_S is further investigated by using other two synthetic examples. We also apply viscoelastic FWI to a field shallow-seismic dataset acquired in Rheinstetten, Germany. An elastic FWI is applied to the same data for comparison. We evaluate the velocity models estimated by viscoelastic FWI by comparing them to a migrated GPR profile.

2 THEORY

2.1 Forward modelling

In order to consider the attenuation into time-domain modelling, the generalized standard linear solid (Liu et al. 1976) is widely applied. It consists of the superposition of several mechanisms (Maxwell bodies) that can be utilized to approximate a nearly constant Q . We adopt a velocity-stress formulation of the viscoelastic wave equation (Robertsson et al. 1994; Blanch et al. 1995; Bohlen 2002; Fabien-Ouellet et al. 2017) as

$$\frac{\partial \sigma_{ij}}{\partial t} = \frac{\partial v_k}{\partial x_k} \left[\frac{M(1 + \tau_P)}{1 + \alpha \tau_P} - \frac{2\mu(1 + \tau_S)}{1 + \alpha \tau_S} \right] \delta_{ij} + \left(\frac{\partial v_i}{\partial x_j} + \frac{\partial v_j}{\partial x_i} \right) \left[\frac{\mu(1 + \tau_S)}{1 + \alpha \tau_S} \right] + \sum_{l=1}^L r_{ijl} + f_{\sigma_{ij}}, \quad (1)$$

$$\rho \frac{\partial v_i}{\partial t} = \frac{\partial \sigma_{ij}}{\partial x_j} + f_{v_i}, \quad (2)$$

$$\frac{\partial r_{ij}}{\partial t} = -\frac{1}{\tau_{\sigma l}} \left[\frac{\partial v_k}{\partial x_k} \left(\frac{M\tau_P}{1 + \alpha \tau_P} - \frac{2\mu\tau_S}{1 + \alpha \tau_S} \right) \delta_{ij} + \left(\frac{\partial v_i}{\partial x_j} + \frac{\partial v_j}{\partial x_i} \right) \frac{\mu\tau_S}{1 + \alpha \tau_S} + r_{ijl} \right], \quad (3)$$

where Einstein summation convention is used here over spatial indices i, j and k ; σ_{ij} is the ij th component of the stress tensor; v_i is the velocity tensor; r_{ij} is the memory variable corresponding to the stress tensor σ_{ij} ; x_i is the i th spatial direction; f is the external force; $\tau_{\sigma l}$ is the stress relaxation time of the l th Maxwell body; L is the total number of Maxwell bodies; τ_S and τ_P are attenuation levels of S wave and P wave, respectively; M and μ are the P-wave and shear modulus, respectively. The parameter α is used to ensure that the waves travel with the model phase velocity at the reference frequency ω_0 (Bohlen 2002). It can be calculated by

$$\alpha = \sum_{l=1}^L \frac{\omega_0^2 \tau_{\sigma l}^2}{1 + \omega_0^2 \tau_{\sigma l}^2}, \quad (4)$$

where the reference frequency ω_0 is set as the peak frequency of the source wavelet (in synthetic examples) or the observed data (in the field example).

The attenuation property of the materials is defined as the ratio between the real and imaginary parts of the complex modulus (O'Connell & Budiansky 1978; Blanch et al. 1995), and the quality

factor can be described as

$$Q = \frac{1 + \sum_{l=1}^L \frac{\omega^2 \tau_{\sigma l}^2}{1 + \omega^2 \tau_{\sigma l}^2} \tau}{\sum_{l=1}^L \frac{\omega \tau_{\sigma l}}{1 + \omega^2 \tau_{\sigma l}^2} \tau}, \quad (5)$$

where ω is the angular frequency, the $\tau_{\sigma l}$ controls the frequency peak locations of the l th Maxwell bodies and is taken as a spatially constant variable before the simulation. The attenuation level τ controls the magnitude of the quality factor (i.e., $\tau \approx \frac{2}{Q}$ when $L = 1$).

A desired constant Q in a limited frequency range can be approximated with different Maxwell bodies (Blanch et al. 1995). Attenuation in viscoelastic media leads to the following frequency dependency of phase velocities of P- and S-waves:

$$V_P^2(\omega) = \frac{M(1 + \tau_P \alpha(\omega))}{\rho(1 + \tau_P \alpha(\omega_0))}, V_S^2(\omega) = \frac{\mu(1 + \tau_S \alpha(\omega))}{\rho(1 + \tau_S \alpha(\omega_0))}. \quad (6)$$

Fig. 1 shows the shape of a desired and the simulated Q values by using only one Maxwell body and the corresponding velocities dispersion for both P and S waves. The constant Q of 10 is well approximated in the frequency band between 10 Hz and 60 Hz, which covers most of the frequency range of shallow-seismic data. Therefore, we only use a single relaxation mechanism in this paper. More than one relaxation mechanism might be necessary if a broader frequency range or stronger attenuation should be considered.

2.2 Full waveform inversion

FWI is an iterative optimization technique that seeks to estimate an optimal subsurface model \mathbf{m} (V_S , V_P , ρ , τ_S , τ_P) by minimizing the difference between the synthetic and observed seismic waveforms. In this paper, we use the least-squares l_2 -error between the true-amplitude (non-normalized) synthetic and observed particle-velocity waveforms as the objective function:

$$\Psi(\mathbf{m}) = \frac{1}{2} \|\mathbf{d}^{syn}(\mathbf{m}) - \mathbf{d}^{obs}\|^2, \quad (7)$$

where $\mathbf{d}^{syn}(\mathbf{m})$ and \mathbf{d}^{obs} are the synthetic and observed particle-velocity seismograms, respectively.

Adjoint state method provides an efficient way to calculate the gradient of misfit function by cross-correlating the forward (state variables) and backward (adjoint state variables) wavefields. The backward wavefields can be calculated by solving the adjoint state equations (Fabien-Ouellet et al. 2017), which can be written as

$$\begin{aligned} \frac{\partial \overleftarrow{\sigma}_{ij}}{\partial t'} = & - \frac{\partial \overleftarrow{v}_k}{\partial x_k} \left[\frac{M(1 + \tau_P)}{1 + \alpha \tau_P} - \frac{2\mu(1 + \tau_S)}{1 + \alpha \tau_S} \right] \delta_{ij} - \left(\frac{\partial \overleftarrow{v}_i}{\partial x_j} + \frac{\partial \overleftarrow{v}_j}{\partial x_i} \right) \frac{\mu(1 + \tau_S)}{1 + \alpha \tau_S} - \sum_{l=1}^L \overleftarrow{r}_{ijl} \\ & + \left[\frac{M(1 + \tau_P)}{1 + \alpha \tau_P} - \frac{2\mu(1 + \tau_S)}{1 + \alpha \tau_S} \right] \delta_{ij} \frac{\partial \Psi}{\partial \sigma_{kk}} + \mu \frac{1 + \tau_S}{1 + \alpha \tau_S} (1 + \delta_{ij}) \frac{\partial \Psi}{\partial \sigma_{ij}} \end{aligned} \quad (8)$$

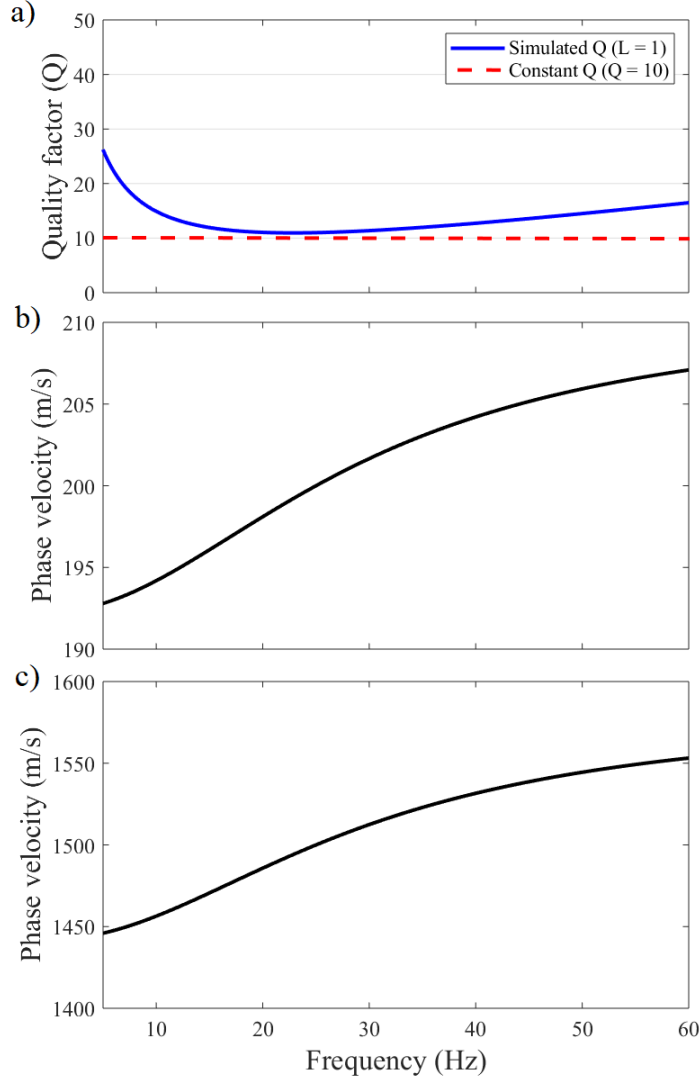


Figure 1. (a) Comparison of a constant Q value (red dashed line) and the Q values simulated by using one relaxation mechanism (blue solid line). (b) Phase velocity dispersion of $V_S = 200$ m/s with $\omega_0 = 2\pi \cdot 25$ Hz. (c) Phase velocity dispersion of $V_P = 1500$ m/s with $\omega_0 = 2\pi \cdot 25$ Hz.

$$\rho \frac{\partial \overleftarrow{v}_i}{\partial t'} = -\frac{\partial \overleftarrow{\sigma}_{ij}}{\partial x_j} + \frac{\partial \Psi}{\partial v_i} \quad (9)$$

$$\frac{\partial \overleftarrow{r}_{ij}}{\partial t'} = -\frac{1}{\tau_{\sigma l}} \left[\frac{\partial \overleftarrow{v}_k}{\partial x_k} \left(\frac{M\tau_P}{1 + \alpha\tau_P} - \frac{2\mu\tau_S}{1 + \alpha\tau_S} \right) \delta_{ij} + \left(\frac{\partial \overleftarrow{v}_i}{\partial x_j} + \frac{\partial \overleftarrow{v}_j}{\partial x_i} \right) \frac{\mu\tau_S}{1 + \alpha\tau_S} + \overleftarrow{r}_{ijl} \right] \quad (10)$$

with $t' = T - t$.

Compared to the forward modelling equations (equations 1-3), the adjoint state equations (equations 8-10) only differ in the source terms and the sign before the spatial derivatives; therefore, they can be solved with the 'same' forward modelling code. Misfit gradients for parameters shear modulus,

P-wave modulus, ρ , τ_S , τ_P are given in Fabien-Ouellet et al. (2017). Then the gradients in terms for V_S , V_P , ρ , τ_S , τ_P can be calculated by applying the chain rule on the Fréchet kernels.

We use a finite-difference method to solve the wave equations and their adjoint state equations (Bohlen 2002). The model parameters are updated iteratively via

$$\mathbf{m}_{k+1} = \mathbf{m}_k + \lambda \delta \mathbf{m}_{k+1}, \quad (11)$$

where the step length λ is calculated by a combination of line search and parabolic fitting. The term $\delta \mathbf{m}_{k+1}$ is the model update direction at the $k + 1$ th iteration, which is calculated via

$$\delta \mathbf{m}_{k+1} = -\mathbf{P} \frac{\partial \Psi}{\partial \mathbf{m}} + \beta \delta \mathbf{m}_k, \quad (12)$$

where the preconditioner \mathbf{P} is calculated by an approximated inverse of the Hessian matrix by using its diagonal term (Plessix & Mulder 2004). The factor β is calculated by a conjugate-gradient method (Hestenes et al. 1952). A multi-scale inversion strategy is used to avoid cycle skipping (Bunks et al. 1995).

3 SYNTHETIC EXAMPLES

In this section, we perform synthetic tests to explore the properties of 2D multi-parameter viscoelastic FWI. We firstly perform two multi-parameter (five-parameters) examples by using a spatially uncorrelated and a spatially correlated model, respectively. Results of viscoelastic and elastic FWIs are also compared. Then we further investigate the crosstalk between coupled parameters V_S and τ_S by comparing multi-parameter (two-parameters) viscoelastic and mono-parameter elastic FWI results.

3.1 Multi-parameter examples

We build a true model that consists of a depth-dependent 1-D background model. A triangular low-value anomaly is superimposed on each parameter model at different positions (Fig. 2). Each triangular anomaly is 8 m wide and 4 m deep. The relative contrast between the anomaly and the background model in the Q models (e.g., $Q_S = 10$ compared with $Q_S \approx 80$) is stronger than the contrasts in the velocity and the density models (e.g., $V_S = 120$ m/s compared with $V_S \approx 180$ m/s, $\rho = 1850$ kg/m³ compared with $\rho \approx 2100$ kg/m³). We use a total of 10 shots with a source spacing of 10 m, starting from $X = 20$ m to $X = 110$ m. The vertical-force source is generated by a delayed Ricker wavelet with a central frequency of 30 Hz. We only use 10 shots to save computational cost. A total of 91 receivers (recording both vertical and horizontal components) are distributed along the free surface with an equidistant spacing of 1 m, starting from $X = 20$ m to $X = 110$ m. The 1-D background models are used as the initial models, and the true source wavelet is used during the inversion. We

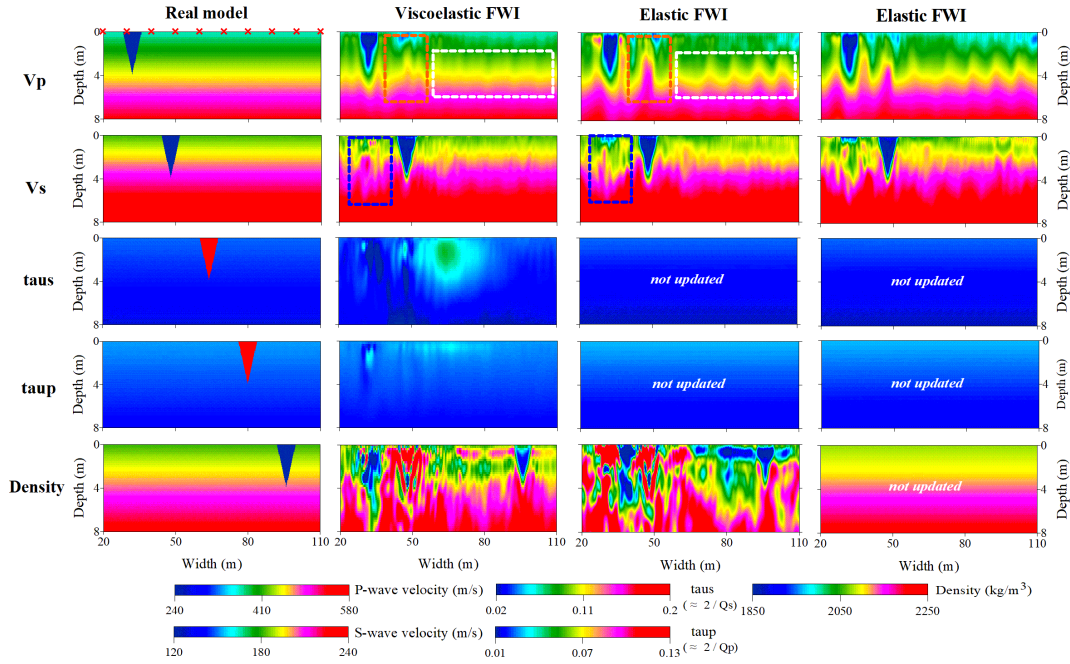


Figure 2. Multi-parameter synthetic example on a spatially uncorrelated model. Four columns represent the true models, viscoelastic FWI results, elastic FWI results for both velocity and density models, and elastic FWI result for velocity models only, respectively. The 1-D background models are used as the initial models for the inversion. The red crosses represent the source locations. Blue and orange rectangles highlight the crosstalk between velocity models.

perform a multi-parameter viscoelastic FWI on the synthetic data in which all five parameters are updated simultaneously during the inversion. A high-cut frequency filter of 25, 35, 45, and 60 Hz is used progressively in the multi-scale strategy. A minimum of 15 iterations are performed at each stage, while the inversion moves to the next stage once the relative improvement in the misfit value becomes less than 1 %.

The reconstructed multi-parameter models show a nice agreement with the true models (first and second columns in Fig. 2), especially for the velocity parameters V_S and V_P . On the contrary, the anomalies in the attenuation models are only roughly reconstructed. In the inverted τ_P model, the triangular anomaly cannot be identified. This reconstruction test shows that viscoelastic FWI is more sensitive to the velocities than the quality factors if we update all parameters simultaneously. Although the triangular anomaly can be easily identified in the reconstructed density model, the density model suffers strong crosstalk from the velocity models at the position where the V_S and V_P anomalies are located, respectively. Furthermore, the density model is also contaminated by strong fluctuations in the shallow part (depth < 4 m).

The reconstructed models show the interactions between the five parameters. V_S has strong crosstalk

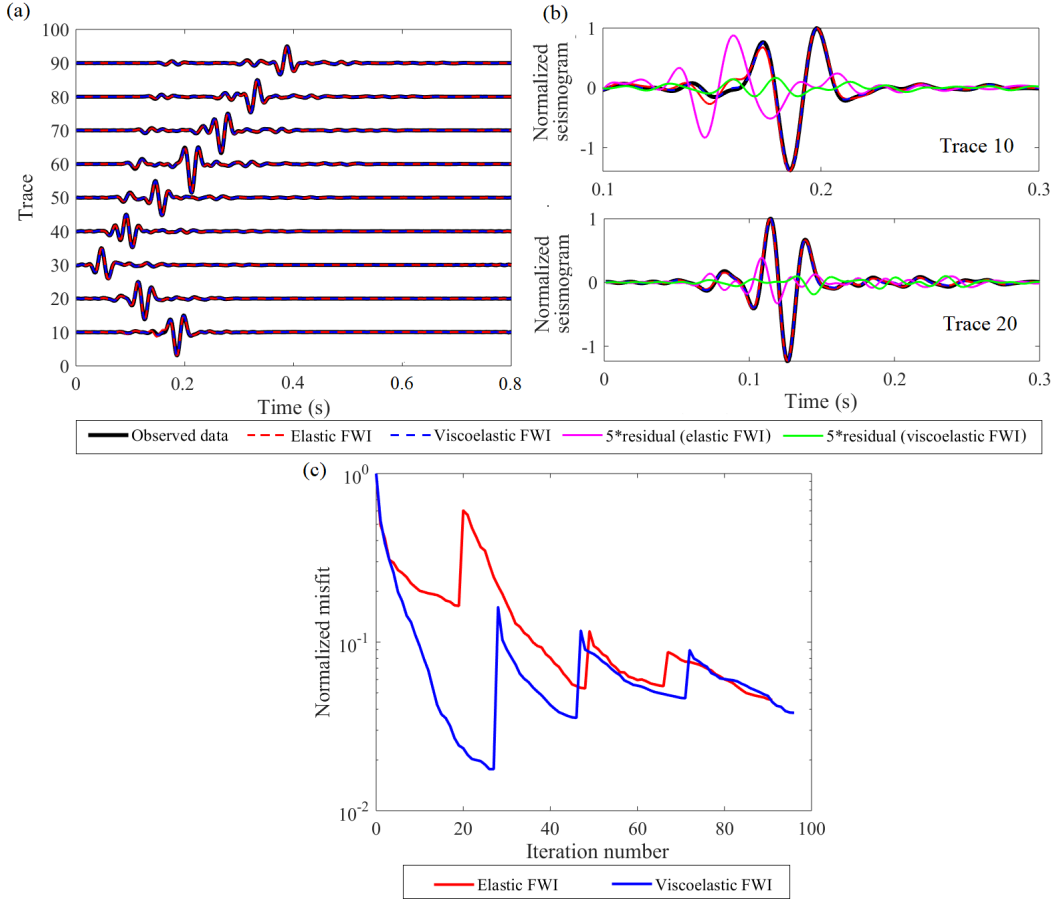


Figure 3. Data fitting in the uncorrelated model (Fig. 2). (a) Comparison of the vertical velocity seismograms of the shot at $X = 50$ m. Thick black lines are the observed seismograms. Red and blue dashed lines are the synthetic seismograms corresponding to the inversion results of multi-parameter elastic and viscoelastic FWIs, respectively. The waveform in each trace is scaled by its offset. (b) upper and lower images show the zoomed comparison for trace 10 and trace 20, respectively. The waveform residual is magnified by 5 times. (c) Comparison of the data misfits in the elastic (red solid line) and viscoelastic FWIs (blue solid line).

to all the other parameters except for τ_P , and only weakly suffers crosstalk from V_P and τ_S . V_P has strong crosstalk to τ_P and density and suffers crosstalk mainly from V_S . The attenuation parameters and the density model suffers strong crosstalk from both V_S and V_P but only weakly produces footprints to the other parameters. Overall, strong crosstalk mainly exists between V_S and V_P , from velocity to attenuation models for the same wave types (i.e., V_S to τ_S , V_P to τ_P), and from both velocities (V_P, V_S) to the density models.

In order to study the importance of considering attenuation, we perform an elastic FWI (Groos et al. 2014) with a fixed Q model on the same dataset. Though named as elastic, the 1D linear-gradient τ models are used in a viscoelastic forward solver but not updated during the inversion (it is some-

times also called 'viscoelastic', 'pseudo-viscoelastic', or 'passive-viscoelastic' FWI since a viscoelastic forward solver is used). Due to the high sensitivity of Rayleigh wave with respect to V_S , the final V_S model is recovered quite robustly. The V_P model reconstructed by elastic FWI contains vertical-stripes artefacts (white square in Fig. 2, wavefront-like artefacts, since the Rayleigh waves mainly propagate horizontally with a vertical wavefront), which do not exist in the viscoelastic FWI result. Because the velocity parameter could not directly cause intrinsic damping in the data, we speculate that these vertical-striped artefacts (scatterers) may arise to imitate the intrinsic anelastic damping by scattering attenuation (Wu 1985; Snieder 1988). The triangular shape of V_P anomaly is less accurately delineated in the elastic FWI result compared to the viscoelastic result. The crosstalk (orange square, Fig. 2) between V_P and V_S becomes stronger in the elastic FWI results since it has fewer parameters to explain the data. Similar but weaker crosstalk can be observed in the reconstructed V_S model (blue square, Fig. 2). This indicates that velocity models can be better recovered when considering the attenuation during the inversion. The density model contains strong artefacts in the shallow part (depth < 4 m) and is worse than the density model reconstructed by viscoelastic FWI. The final synthetic shot gathers in both the elastic and viscoelastic FWIs show a nice agreement with the observed data (Fig. 3a). The waveform residual in the viscoelastic FWI result is hardly visible and is smaller than the elastic FWI result (Fig. 3b and c).

We conduct another elastic FWI by fixing both density and attenuation models, in which similar velocity models are estimated (fourth column, Fig. 2). It indicates that surface-wave FWI is not very sensitive to the density model. Elastic and viscoelastic FWI produce a very similar V_S model, indicating that V_S can be recovered well if a smooth background Q model is used. However, the viscoelastic FWI results contain weaker artefacts in the secondary parameters such as V_P and density, compared to the elastic FWI with passive attenuation model. Worse results in V_S would be obtained if we would fully ignore attenuation effects and just perform purely elastic forward modelling in the FWI workflow (Groos et al. 2014).

In the second experiment, we assume that the parameter perturbations are located at the same position (first column, Fig. 4). This spatially correlated model is generally more realistic compared to the previous one since all the physical-parameter anomalies usually belong to the same geological target. The same acquisition geometry, initial models, and inversion parameters as in the first example are used. Similarly, we also perform both viscoelastic and elastic FWIs on the same dataset for comparison.

All five parameter models are nicely reconstructed in the viscoelastic FWI results (second column in Fig. 4). The triangular shape of the anomaly is better delineated in the V_S model compared to the V_P model. We can see the location of the anomaly in both τ_S and τ_P with a more accurate estimation

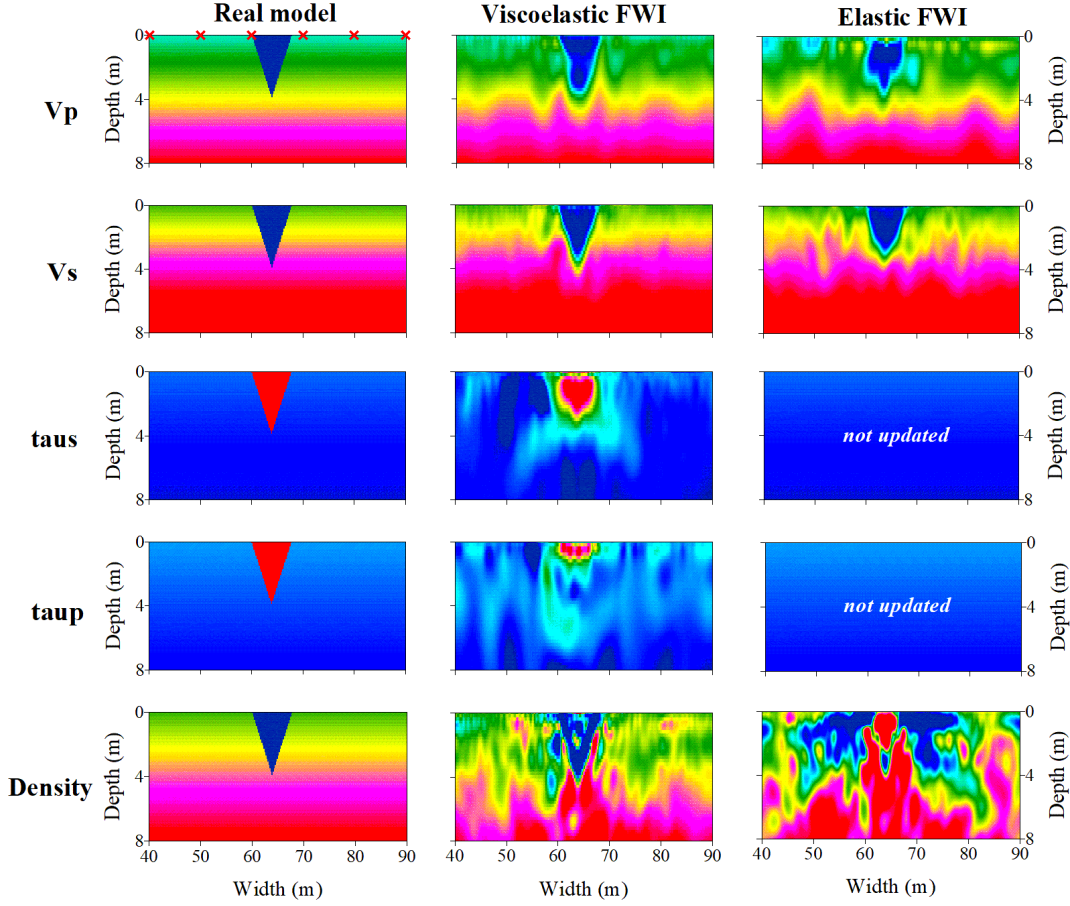


Figure 4. Multi-parameter synthetic example on a spatially correlated model. Three columns represent the true models, viscoelastic FWI results, and elastic FWI results, respectively. The 1-D background models are used as the initial models for the inversion. All the colour scales are identical to Fig. 2. The red crosses represent the source locations.

of the values compared with the spatially-uncorrelated example. Although the anomaly is visible in the density model, it suffers from much stronger artefacts compared to the other parameter models.

The elastic FWI with fixed Q models also resolves the location and the velocity structure of the anomaly (third column in Fig. 4). The triangular shapes of both V_P and V_S anomalies (especially for V_P), however, are worse delineated compared to the viscoelastic FWI results. The reconstructed density model shows a wrong result in which a high-density anomaly instead of the low-density anomaly is reconstructed. Similar to the previous example, both viscoelastic and elastic FWI nicely fit the observed data, while a smaller data misfit is obtained by viscoelastic FWI compared to elastic FWI (Fig. 5).

Overall, both two synthetic experiments show that the reconstruction of V_S is quite robust regardless of whether viscoelastic or elastic FWI is adopted. The viscoelastic FWI provides more accurate and comprehensive results compared to elastic FWI, especially for the reconstruction of V_P . The effect

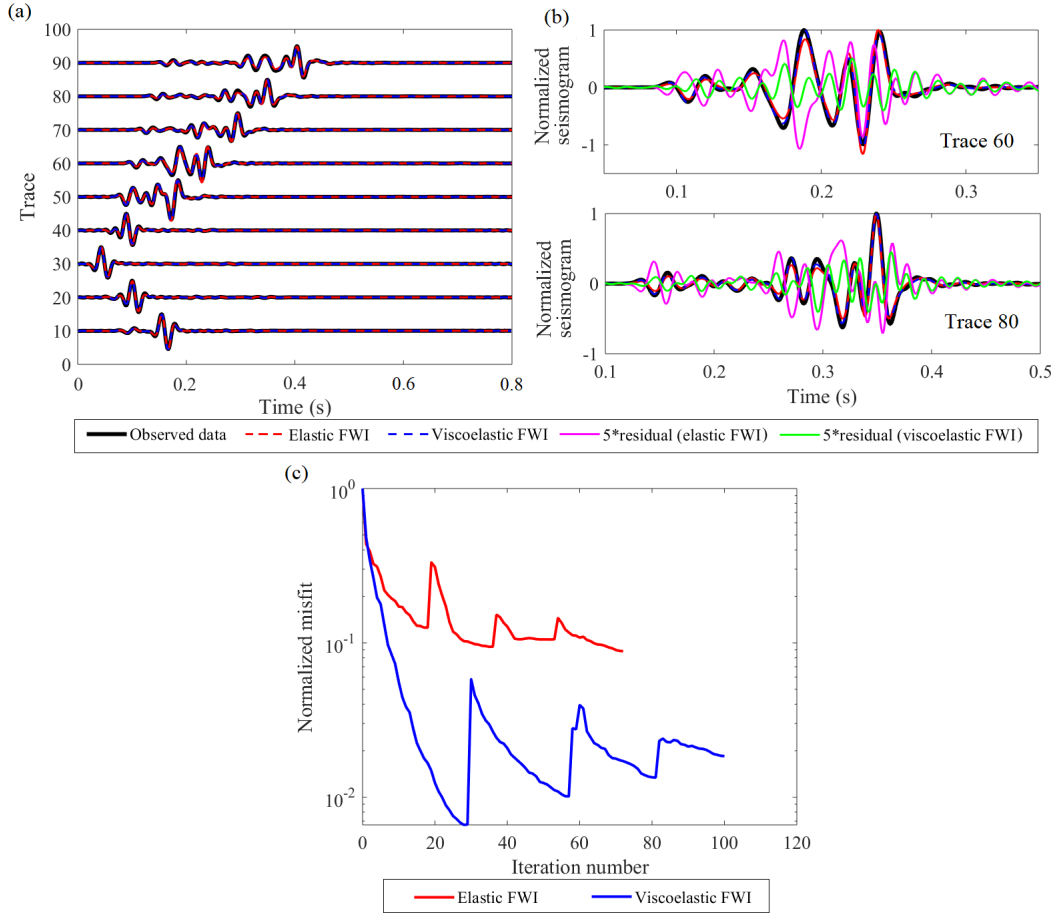


Figure 5. Data fitting in the correlated model (Fig. 4). (a) Comparison of the vertical velocity seismograms of the shot at $X = 50$ m. Thick black lines are the observed seismograms. Red and blue dashed lines are the synthetic seismograms corresponding to the inversion results of multi-parameter elastic and viscoelastic FWIs, respectively. The waveform in each trace is scaled by its offset. (b) upper and lower images show the zoomed comparison for trace 60 and trace 80, respectively. The waveform residual is magnified by 5 times. (c) Comparison of the data misfits in the elastic (red solid line) and viscoelastic FWI (blue solid line).

of attenuation is contaminated by the footprint from the velocity, while the velocity is relatively less affected by the attenuation.

3.2 Crosstalk between coupled velocity and quality factor

We perform another two synthetic tests to investigate the crosstalk between coupled parameters: V_S and τ_S . We use the same 1D background models for velocities and quality factors, but only superimpose a low- V_S anomaly and a low- Q_S (high- τ_S) anomaly at different positions (first column, Fig. 6). We add a water table at 10 m depth, and the P-wave velocity below the water table is set to 1500 m/s. A homogeneous density model with a value of 2050 kg/m³ is used. A total of seven vertical-force

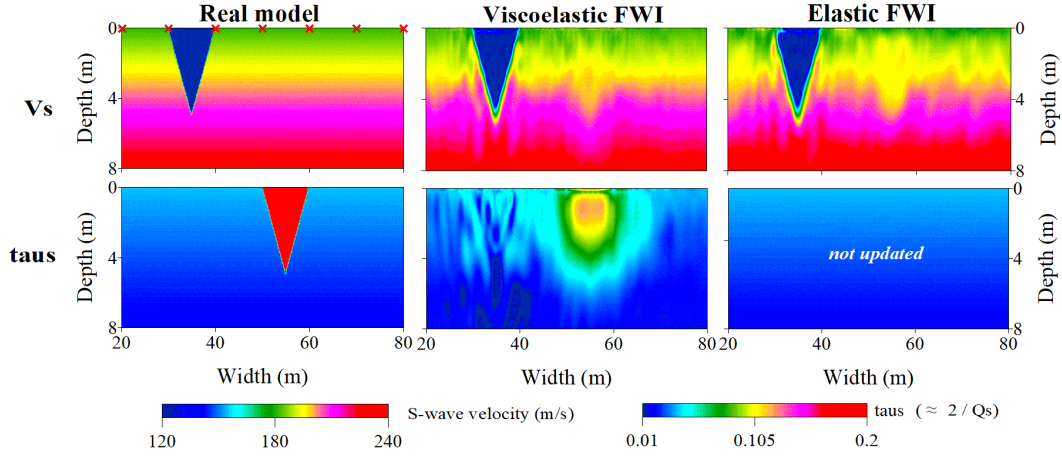


Figure 6. Two-parameter synthetic example on a spatially uncorrelated model. Three columns are the true models, two-parameter viscoelastic FWI results, and mono-parameter elastic FWI result, respectively. The red crosses represent the source locations.

sources are placed with a spacing of 10 m from $X = 20$ m to $X = 80$ m. The sources are generated with a delayed Ricker wavelet of 30 Hz. A total of 61 two-component receivers are distributed along the free surface with an equidistant spacing of 1 m from the first to the last source positions. The 1-D background models are used as the initial models, and we only update V_S and τ_S models during the inversion.

In the spatially uncorrelated test, the reconstructed V_S model by viscoelastic FWI (second column in Fig. 6) shows a nice agreement with the true model and is slightly affected by the τ_S anomaly. On the contrary, the τ_S model is only roughly reconstructed and the value of τ_S anomaly is underestimated. Besides, it is contaminated by a strong footprint from the V_S anomaly. The poor reconstruction of the τ_S anomaly confirms the high sensitivity of V_S .

For comparison, we perform an elastic FWI by adopting and keeping the background τ_S model during the inversion. The reconstructed V_S model matches the true model satisfactorily (third column, Fig. 6). It clearly delineates the location, shape and the value of the V_S anomaly. Nevertheless, the reconstructed V_S model suffers stronger crosstalk from the τ_S anomaly compared to the results of viscoelastic FWI. Strong vertically orientated artefacts are also observed.

Similarly, we perform a synthetic test on a spatially correlated model in which V_S and τ_S anomalies locate at the same location (first column in Fig. 7). Both V_S and τ_S models are successfully recovered by viscoelastic FWI. In the result of elastic FWI, however, strong artefacts and distortion appear in the surrounding area of the anomaly (third column, Fig. 7). These artefacts behave as vertical-stripped anomalies, which are parallel to the wavefront of Rayleigh-wave. The shape of the τ_S anomaly is nicely delineated and more accurate compared to the spatially uncorrelated example. Overall, these

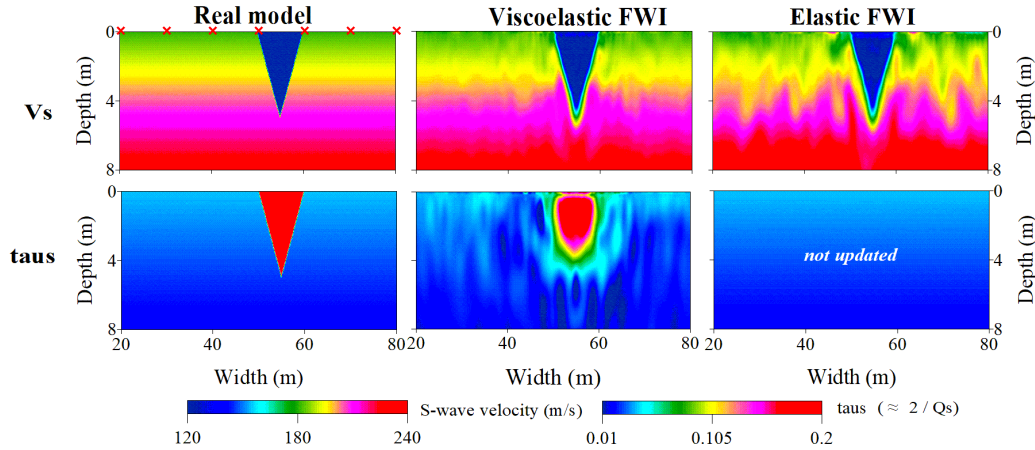


Figure 7. Two-parameter synthetic example on a spatially correlated model. Three columns are the true models, two-parameter viscoelastic FWI results, and mono-parameter elastic FWI result, respectively. The red crosses represent the locations of the sources.

two examples again show that the multi-parameter viscoelastic FWI provides better result compared to the elastic FWI. If we do not invert for attenuation, the heterogeneity in Q_S may be projected into the reconstructed V_S model.

4 APPLICATION TO FIELD DATA

We apply the multi-parameter viscoelastic FWI strategy to a shallow seismic field dataset. The test site is located on a glider airfield in Rheinstetten, Germany. The shallow subsurface is composed of fluvial sediments from the late Pleistocene. A refilled trench, namely "Ettlinger Linie" (EL), is approximately located in the middle of our survey line (Wittkamp et al. 2019). The seismic dataset is excited by vertical hammer blows and recorded by 48 multi-component geophones spaced every 1 m. Although multi-component data outperforms single-component data in 2D FWI (Nuber et al. 2017), we only use vertical-component data in our example because the horizontal-component data has a relatively low signal-to-noise ratio. A total of 12 shots with a 4-m spacing are used (asterisks in Fig. 8). The first source position is located between the first and second geophones. Furthermore, 3D to 2D transformation (Forbriger et al. 2014) is necessary before the FWI because we only use a 2D forward solver. Schäfer et al. (2014) proved the applicability of this 3D to 2D transformation to heterogeneous models.

We use surface-wave methods to build the initial models for FWI to reduce the possibility of cycle skipping (1st column in Fig. 8). 1D V_S and Q_S models are estimated by the inversions of Rayleigh-wave dispersion curve and attenuation coefficients (Gao et al. 2018), respectively. The initial 1D V_P model is estimated by first-arrival traveltimes inversion. It consists of two layers with sharp velocity

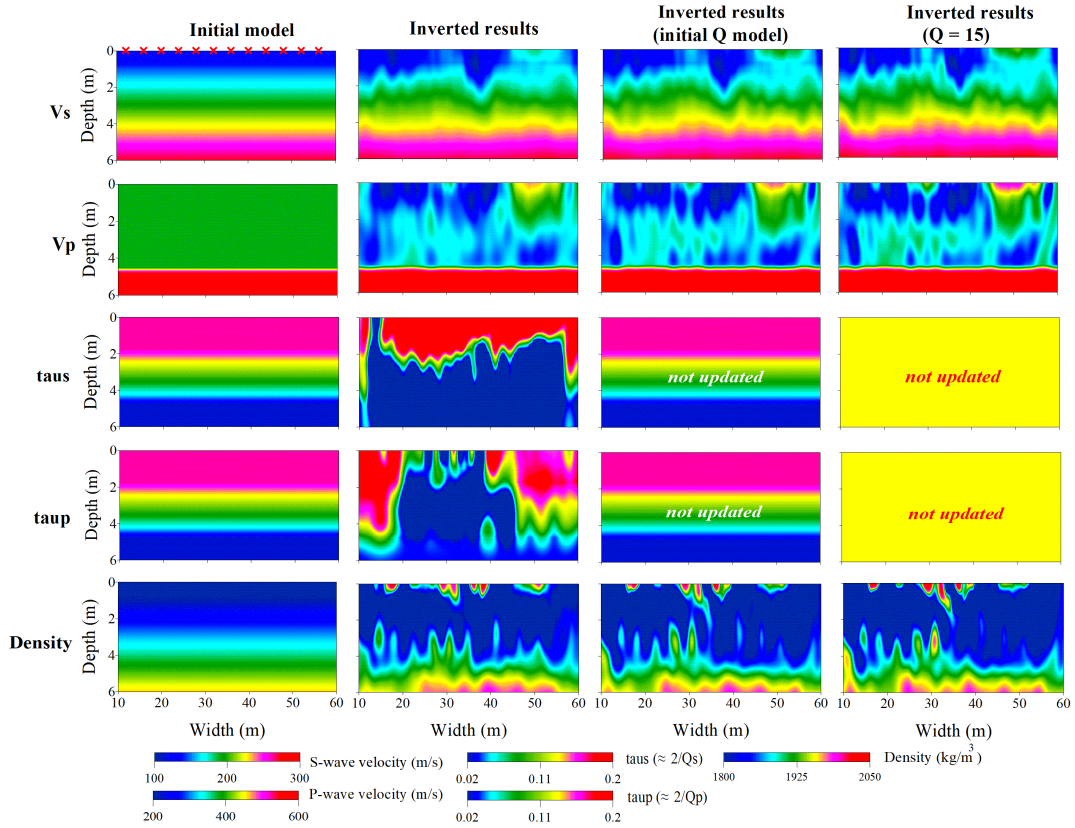


Figure 8. Comparison of reconstructed models in the field example. The first column represents the initial models. The second column shows the inversion results of multi-parameter viscoelastic FWI. The third and fourth columns show the inversion results obtained by multi-parameter elastic FWI without updating the Q model. The fixed Q models for the third and fourth columns are the depth-dependent and homogeneous Q models, respectively. The red crosses represent the locations of the sources.

contrast at a depth around 6 m which corresponds to the groundwater table (Pasquet et al. 2015; Wittkamp et al. 2019). For the initial Q_P model $Q_P = Q_S$ is assumed. A linear gradient model is used as the initial density model.

The multi-scale strategy starts with low-pass filtered data up to 10 Hz. The frequency content is progressively increased by 5 Hz until 60 Hz is reached. A minimum of three iterations is guaranteed in each stage, and the inversion moved to the next stage when the relative decrease in the misfit value is less than 1%. We estimate a wavelet correction filter by a stabilized deconvolution (Groos et al. 2014) and use it to update the source time function at the beginning of each stage.

The multi-parameter inversion results are shown in the 2nd column in Fig. 8. The inverted V_S model shows a triangular low-velocity anomaly in the central part of the spread, indicating the existence and the location of the EL. A similar low-velocity anomaly can also be identified in the final V_P model. The τ_S and τ_P models show relatively high τ values (low Q values with $Q < 15$) in the shallow

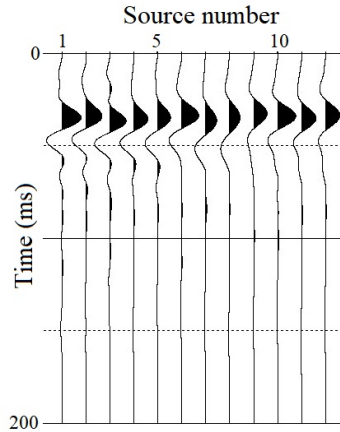


Figure 9. The estimated source time functions of the twelve shot gathers.

subsurface (top 2 m), and relatively lower τ values (higher Q values) in the deeper part. It indicates that the attenuation in seismic waves is mainly caused by the shallow soil (weathering zone). The final density model doesn't provide geological information about the trench, which may be caused by the relatively low sensitivity of Rayleigh waves with respect to density. Overall, the inversion of the field data provides a relatively high resolution in the velocity models and a relatively low resolution in the Q and density models. Twelve inverted source time functions (Fig. 9) show a similar shape among each other, indicating that estimated source time functions are fairly reliable. It is worth mentioning that the final wavelet does not necessarily represent the actual source wavelet excited in the field measurement, instead, it also accounts for the residual caused by the inaccurate inversion result. The synthetic waveforms fit the observed data fairly well (Fig. 10), which indicates a successful explanation of the observed wavefield by the final multi-parameter models.

In order to study the role of attenuation for the Rheinstetten study area, we also perform elastic FWI tests on the same data by using a fixed initial depth-dependent Q model and a homogeneous Q model during the inversion (third and fourth columns in Fig. 8), respectively. The inverted V_S and V_P models show a similar low-velocity anomaly. However, they are contaminated with vertical-striped artefacts, which is mainly caused by ignoring the heterogeneity in the Q models. Similar artefacts have also been observed in our synthetic reconstruction tests. The existence of the artefacts makes it difficult to identify the shape of the EL in the reconstructed P-wave velocity model.

To validate our final FWI results, we compare our velocity models obtained by viscoelastic FWI (2nd column in Fig. 8) to a migrated GPR profile (Wittkamp et al. 2019) acquired along the same survey line (Fig. 11). The comparison with the GPR section shows a fairly good agreement concerning the location and the shape of the EL. It verifies fairly high reliability of the final S- and P-wave velocity models estimated by the multi-parameter viscoelastic FWI.

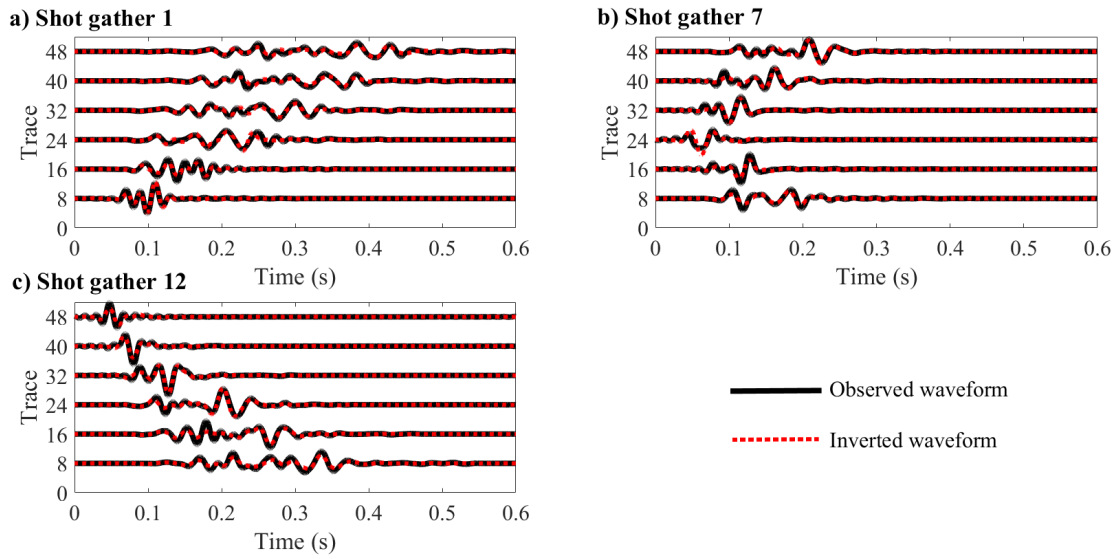


Figure 10. Comparison of vertical velocity seismograms in the first, seventh, and last shots. Thick black lines are the observed seismograms. Red dashed lines are the synthetic seismograms corresponding to the inversion results of multi-parameter viscoelastic FWI. The waveform in each trace is scaled by its offset.

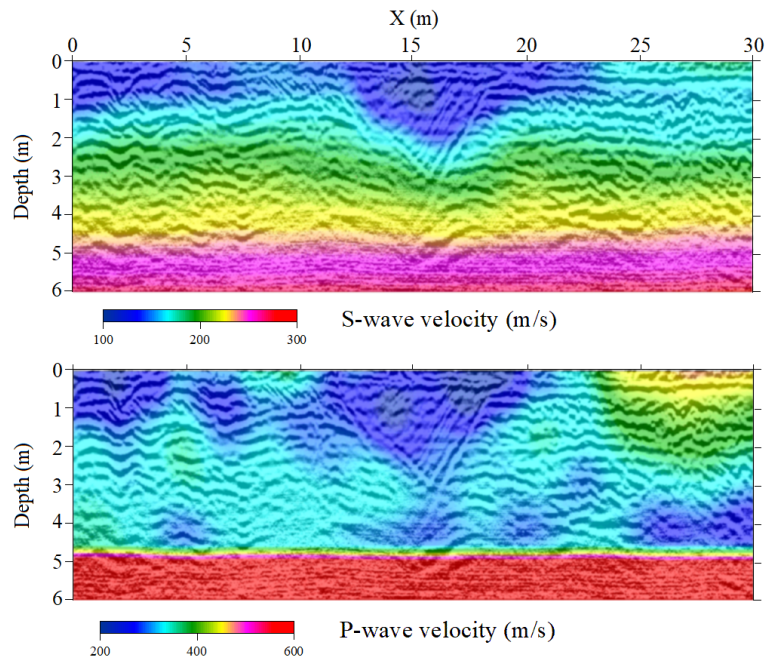


Figure 11. Comparison between the field-data inversion results and a GPR profile. The S-wave velocity and P-wave velocity models are overlying on the migrated image of the GPR measurement.

5 DISCUSSION

In the field-data application, the elastic FWIs also nicely reconstruct the S-wave velocity models because we adopt good passive Q models in the elastic FWI. It indicates that the availability of a sufficiently good passive Q model allows reconstruction of a reliable S-wave velocity model. Poor results will be obtained if we use the purely elastic FWI without any prior information of attenuation (Groos et al. 2014). Nevertheless, the numerical tests show that, when encountering heterogeneous Q model, multi-parameter viscoelastic FWI can further improve the accuracy of estimated velocity model and is superior to elastic FWI in which attenuation is considered as a passive modelling parameter only. In our field example, a similar improvement in the accuracy of the inversion result is also observed, especially for the reconstruction of the P-wave velocity model. Besides, the reconstructed Q models might also be helpful for geological interpretation. Therefore, it is meaningful to incorporate attenuation into the inversion for reconstructing accurate multi-parameter results to better delineate the subsurface structures and properties, especially when the Q model is highly heterogeneous.

In general, the resolution of the estimated Q models in viscoelastic FWI is much poorer compared to the resolution of the velocity models. Only one relaxation mechanism has been used in this study to describe the frequency dependency of Q for the sake of computational cost. Since we only use single relaxation mechanism, the estimated Q values might be lower than their true values (Fig. 1). The importance of considering multiple relaxation mechanisms needs to be further investigated in the future.

Multi-parameter inversion including seismic velocities and quality factors of both P- and S-waves can provide more comprehensive information to improve the characterization of the shallow subsurface. However, the inversion results might be contaminated by crosstalk between the perturbations of different parameters, which decreases the reliability of the reconstructed models. In this paper, we use a preconditioned conjugate gradient algorithm to invert the data, which cannot reduce the parameter trade-off between coupled parameters appropriately. The utilizing of second-order optimization algorithm (Operto et al. 2013; Métivier et al. 2013) for reducing parameter trade-offs in the viscoelastic FWI of shallow-seismic data needs to be further investigated.

6 CONCLUSIONS

We applied 2D multi-parameter viscoelastic full-waveform inversion (FWI) to shallow-seismic surface waves. We tested the capability of this method to reconstruct reliable parameters on synthetic datasets with spatially correlated and uncorrelated models. The synthetic results of spatially uncorrelated models showed that shallow-seismic data has the highest sensitivity with respect to V_S , then

V_P , and relatively low sensitivity to density, Q_S and Q_P . They also showed that crosstalk mainly exists between velocity models (i.e., V_S and V_P) and coupled velocity-quality factor pairs (i.e., V_S and Q_S , V_P and Q_P). Crosstalk between coupled parameters V_S and τ_S was further investigated by another two synthetic examples in which strong crosstalk from V_S to τ_S is observed. If attenuation is not updated, artefacts in the estimated velocity models may be developed. Overall, all these synthetic examples showed that multi-parameter viscoelastic FWI provides more accurate and comprehensive multi-parameter results compared to the elastic FWI, especially for the reconstruction of the P-wave velocity model.

We also applied the multi-parameter viscoelastic FWI approach to a field shallow-seismic dataset acquired in Rheinstetten, Germany. The final V_S and V_P models revealed a sharp triangular low-velocity anomaly, which accurately delineates the location and the shape of a known refilled trench. We compared our viscoelastic FWI result to the results estimated by elastic FWI in which Q models were included but not updated during the inversion. Although the elastic results could also reveal the triangular low-velocity anomaly in the V_S models, they were contaminated by vertical-striped artefacts, which was mainly caused by the neglecting of heterogeneity in the Q models. A good agreement between our viscoelastic FWI result and a migrated GPR profile verified the accuracy of our estimated models and validity of the method. Mitigation of crosstalk between coupled parameters needs to be studied in the future.

ACKNOWLEDGMENTS

The authors thank the editor Hervé Chauris and two anonymous reviewers for their constructive comments. This work was funded by the Deutsche Forschungsgemeinschaft (DFG, German Research Foundation) – Project-ID 258734477 – SFB 1173.

REFERENCES

- Bai, T., Tsvankin, I., & Wu, X., 2017. Waveform inversion for attenuation estimation in anisotropic media, *Geophysics*, **82**(4), WA83–WA93.
- Bergamo, P., Boiero, D., & Socco, L. V., 2012. Retrieving 2D structures from surface-wave data by means of space-varying spatial windowing, *Geophysics*, **77**(4), EN39–EN51.
- Blanch, J. O., Robertsson, J. O., & Symes, W. W., 1995. Modeling of a constant Q: Methodology and algorithm for an efficient and optimally inexpensive viscoelastic technique, *Geophysics*, **60**(1), 176–184.
- Boaga, J., Cassiani, G., Strobbia, C. L., & Vignoli, G., 2013. Mode misidentification in Rayleigh waves: Ellipticity as a cause and a cure, *Geophysics*, **78**(4), EN17–EN28.

- Bohlen, T., 2002. Parallel 3-D viscoelastic finite difference seismic modelling, *Computers & Geosciences*, **28**(8), 887–899.
- Bohlen, T., Kugler, S., Klein, G., & Theilen, F., 2004. 1.5D inversion of lateral variation of Scholte wave dispersion, *Geophysics*, **69**(2), 330–344.
- Brossier, R., 2011. Two-dimensional frequency-domain visco-elastic full waveform inversion: Parallel algorithms, optimization and performance, *Computers & Geosciences*, **37**(4), 444–455.
- Bunks, C., Saleck, F. M., Zaleski, S., & Chavent, G., 1995. Multiscale seismic waveform inversion, *Geophysics*, **60**(5), 1457–1473.
- Carcione, J. M., Kosloff, D., & Kosloff, R., 1988. Wave propagation simulation in a linear viscoelastic medium, *Geophysical Journal International*, **95**(3), 597–611.
- Fabien-Ouellet, G., Gloaguen, E., & Giroux, B., 2017. Time domain viscoelastic full waveform inversion, *Geophysical Journal International*, **209**(3), 1718–1734.
- Forbriger, T., Groos, L., & Schäfer, M., 2014. Line-source simulation for shallow-seismic data. Part 1: Theoretical background, *Geophysical Journal International*, **198**(3), 1387–1404.
- Gao, L., Xia, J., & Pan, Y., 2014. Misidentification caused by leaky surface wave in high-frequency surface wave method, *Geophysical Journal International*, **199**(3), 1452–1462.
- Gao, L., Xia, J., Pan, Y., & Xu, Y., 2016. Reason and condition for mode kissing in MASW method, *Pure and Applied Geophysics*, **173**(5), 1627–1638.
- Gao, L., Pan, Y., Tian, G., & Xia, J., 2018. Estimating Q factor from multi-mode shallow-seismic surface waves, *Pure and Applied Geophysics*, **175**(8), 2609–2622.
- Groos, L., Schäfer, M., Forbriger, T., & Bohlen, T., 2014. The role of attenuation in 2D full-waveform inversion of shallow-seismic body and Rayleigh waves, *Geophysics*, **79**(6), R247–R261.
- Groos, L., Schäfer, M., Forbriger, T., & Bohlen, T., 2017. Application of a complete workflow for 2D elastic full-waveform inversion to recorded shallow-seismic Rayleigh waves, *Geophysics*, **82**(2), R109–R117.
- Hayashi, K. & Suzuki, H., 2004. CMP cross-correlation analysis of multi-channel surface-wave data, *Exploration Geophysics*, **35**(0), 7–13.
- Hestenes, M. R., Stiefel, E., et al., 1952. Methods of conjugate gradients for solving linear systems, *Journal of research of the National Bureau of Standards*, **49**(6), 409–436.
- Ikeda, T., Tsuji, T., & Matsuoka, T., 2013. Window-controlled CMP crosscorrelation analysis for surface waves in laterally heterogeneous media, *Geophysics*, **78**(6), EN95–EN105.
- Irnaka, T., Brossier, R., Métivier, L., Bohlen, T., & Pan, Y., 2019. Towards 3D 9C elastic full waveform inversion of shallow seismic wavefields - Case study Ettlingen Line, in *81st EAGE Conference and Exhibition 2019*.
- Kamei, R. & Pratt, R., 2013. Inversion strategies for visco-acoustic waveform inversion, *Geophysical Journal International*, **194**(2), 859–884.
- Liu, H.-P., Anderson, D. L., & Kanamori, H., 1976. Velocity dispersion due to anelasticity; implications for seismology and mantle composition, *Geophysical Journal International*, **47**(1), 41–58.

- Malinowski, M., Operto, S., & Ribodetti, A., 2011. High-resolution seismic attenuation imaging from wide-aperture onshore data by visco-acoustic frequency-domain full-waveform inversion, *Geophysical Journal International*, **186**(3), 1179–1204.
- Masoni, I., Boelle, J.-L., Brossier, R., & Virieux, J., 2016. Layer stripping FWI for surface waves, in *SEG Technical Program Expanded Abstracts 2016*, pp. 1369–1373, Society of Exploration Geophysicists.
- Métivier, L., Brossier, R., Virieux, J., & Operto, S., 2013. Full waveform inversion and the truncated Newton method, *SIAM Journal on Scientific Computing*, **35**(2), B401–B437.
- Mirzanejad, M. & Tran, K. T., 2019. 3D viscoelastic full waveform inversion of seismic waves for geotechnical site investigation, *Soil Dynamics and Earthquake Engineering*, **122**, 67–78.
- Mora, P., 1987. Nonlinear two-dimensional elastic inversion of multioffset seismic data, *Geophysics*, **52**(9), 1211–1228.
- Nuber, A., Manukyan, E., & Maurer, H., 2017. Optimizing measurement geometry for seismic near-surface full waveform inversion, *Geophysical Journal International*, **210**(3), 1909–1921.
- O’Connell, R. & Budiansky, B., 1978. Measures of dissipation in viscoelastic media, *Geophysical Research Letters*, **5**(1), 5–8.
- Operto, S., Gholami, Y., Prieux, V., Ribodetti, A., Brossier, R., Métivier, L., & Virieux, J., 2013. A guided tour of multiparameter full-waveform inversion with multicomponent data: From theory to practice, *The Leading Edge*, **32**(9), 1040–1054.
- Pan, Y., Xia, J., Xu, Y., Gao, L., & Xu, Z., 2016. Love-wave waveform inversion for shallow shear-wave velocity using a conjugate gradient algorithm, *Geophysics*, **81**(1), R1–R14.
- Pan, Y., Gao, L., & Bohlen, T., 2018. Time-domain full-waveform inversion of Rayleigh and Love waves in presence of free-surface topography, *Journal of Applied Geophysics*, **152**, 77 – 85.
- Pan, Y., Gao, L., & Bohlen, T., 2019. High-resolution characterization of near-surface structures by surface-wave inversions: from dispersion curve to full waveform, *Surveys in Geophysics*, **40**(2), 167–195.
- Pan, Y., Gao, L., & Shigapov, R., 2020. Multi-objective waveform inversion of shallow seismic wavefields, *Geophysical Journal International*, **220**(3), 1619–1631.
- Pasquet, S., Bodet, L., Dhemaied, A., Mouhri, A., Vitale, Q., Rejiba, F., Flipo, N., & Guérin, R., 2015. Detecting different water table levels in a shallow aquifer with combined P-, surface and SH-wave surveys: Insights from VP/Vs or Poisson’s ratios, *Journal of Applied Geophysics*, **113**, 38–50.
- Pérez Solano, C., Donno, D., & Chauris, H., 2014. Alternative waveform inversion for surface wave analysis in 2-D media, *Geophysical Journal International*, **198**(3), 1359–1372.
- Plessix, R.-E. & Mulder, W., 2004. Frequency-domain finite-difference amplitude-preserving migration, *Geophysical Journal International*, **157**(3), 975–987.
- Robertsson, J. O., Blanch, J. O., & Symes, W. W., 1994. Viscoelastic finite-difference modeling, *Geophysics*, **59**(9), 1444–1456.
- Romdhane, A., Grandjean, G., Brossier, R., Rejiba, F., Operto, S., & Virieux, J., 2011. Shallow-structure characterization by 2D elastic full waveform inversion, *Geophysics*, **76**(3), R81–R93.

- Schäfer, M., Groos, L., Forbriger, T., & Bohlen, T., 2014. Line-source simulation for shallow-seismic data. part 2: full-waveform inversion—a synthetic 2-D case study, *Geophysical Journal International*, **198**(3), 1405–1418.
- Snieder, R., 1988. The optical theorem for surface waves and the relation with surface-wave attenuation, *Geophysical Journal International*, **95**(2), 293–302.
- Socco, L., Boiero, D., Foti, S., & Wisén, R., 2009. Laterally constrained inversion of ground roll from seismic reflection records, *Geophysics*, **74**(6), G35–G45.
- Socco, L., Foti, S., & Boiero, D., 2010. Surface wave analysis for building near surface velocity models: established approaches and new perspectives, *Geophysics*, **75**(5), A83–A102.
- Tarantola, A., 1984. Inversion of seismic reflection data in the acoustic approximation, *Geophysics*, **49**(8), 1259–1266.
- Tran, K., McVay, M., Faraone, M., & Horhota, D., 2013. Sinkhole detection using 2D full seismic waveform tomography, *Geophysics*, **78**(5), R175–R183.
- Virieux, J. & Operto, S., 2009. An overview of full-waveform inversion in exploration geophysics, *Geophysics*, **74**(6), WCC1–WCC26.
- Wittkamp, F., Athanasopoulos, N., & Bohlen, T., 2019. Individual and joint 2-D elastic full-waveform inversion of Rayleigh and Love waves, *Geophysical Journal International*, **216**(1), 350–364.
- Wu, R.-S., 1985. Multiple scattering and energy transfer of seismic waves - separation of scattering effect from intrinsic attenuation - I. Theoretical modelling, *Geophysical Journal of the Royal Astronomical Society*, **82**(1), 57–80.
- Wu, R.-S., Luo, J., & Wu, B., 2014. Seismic envelope inversion and modulation signal model, *Geophysics*, **79**(3), WA13–WA24.
- Xia, J., Miller, R., & Park, C., 1999. Estimation of near-surface shear-wave velocity by inversion of Rayleigh wave, *Geophysics*, **64**(4), 691–700.
- Xia, J., Miller, R. D., Park, C. B., & Tian, G., 2002. Determining Q of near-surface materials from Rayleigh waves, *Journal of Applied Geophysics*, **51**(2), 121 – 129.
- Xing, Z. & Mazzotti, A., 2019. Two-grid full-waveform Rayleigh-wave inversion via a genetic algorithm—Part 1: Method and synthetic examples, *Geophysics*, **84**(5), R805–R814.
- Yang, P., Brossier, R., Métivier, L., & Virieux, J., 2016. A review on the systematic formulation of 3-D multiparameter full waveform inversion in viscoelastic medium, *Geophysical Journal International*, **207**(1), 129–149.
- Yuan, Y. O., Simons, F. J., & Bozdağ, E., 2015. Multiscale adjoint waveform tomography for surface and body waves, *Geophysics*, **80**(5), R281–R302.